

PAPER

Hall physics during magnetic reconnection with collision effect

To cite this article: Yukang Shu *et al* 2024 *Plasma Phys. Control. Fusion* **66** 045011

View the [article online](#) for updates and enhancements.

You may also like

- [A Parametric Study of the Structure of Hall Magnetic Field Based on Kinetic Simulations. I. Anti-parallel Magnetic Reconnection in an Asymmetric Current Sheet](#)
Longlong Sang, Quanming Lu, Rongsheng Wang et al.
- [On the signatures of magnetic islands and multiple X-lines in the solar wind as observed by ARTEMIS and WIND](#)
S Eriksson, D L Newman, G Lapenta et al.
- [Multiple X-line Reconnection Observed in Mercury's Magnetotail Driven by an Interplanetary Coronal Mass Ejection](#)
J. Zhong, L. C. Lee, X. G. Wang et al.

Hall physics during magnetic reconnection with collision effect

Yukang Shu¹ , San Lu^{2,3,4,*}, Quanming Lu^{2,3,4,*}, Kai Huang^{2,3,4} , Rongsheng Wang^{2,3,4} and Weixing Ding¹

¹ School of Nuclear Science and Technology, University of Science and Technology of China, Hefei, Anhui, People's Republic of China

² CAS Key Laboratory of Geospace Environment, School of Earth and Space Sciences, University of Science and Technology of China, Hefei, Anhui, People's Republic of China

³ CAS Center for Excellence in Comparative Planetology, Hefei, Anhui, People's Republic of China

⁴ Collaborative Innovation Center of Astronautical Science and Technology, Harbin 150001, People's Republic of China

E-mail: lusan@ustc.edu.cn and qmlu@ustc.edu.cn

Received 23 November 2023, revised 24 January 2024

Accepted for publication 21 February 2024

Published 1 March 2024



CrossMark

Abstract

The Hall effect, decoupling between the ion and electron motions, is the core mechanism triggering fast reconnection. In plasmas with collision effects such as laboratory facilities, collision can suppress the Hall effect and influence the triggering of fast reconnection. Here, by conducting a series of kinetic simulations with varying collision parameters, we show that collisions can suppress the electron outflow, impairing the quadrupole Hall magnetic field. Besides, collision weakens the inflow of magnetic flux by reducing the charge separation and increasing the thermal pressure at the reconnection site, leading to a reduction of the Hall electric field. As the collisionality becomes larger, the Hall electric field diminishes more easily than the Hall magnetic field. We propose that the quadrupolar Hall magnetic field can be a significant indicator in reflecting Hall reconnection.

Keywords: magnetic reconnection, Hall effect, collision

1. Introduction

As a ubiquitous process in space plasmas and laboratory facilities, magnetic reconnection leads to topological changes in the magnetic field and converts magnetic energy to kinetic energy, resulting in plasma accelerating and heating. Magnetic reconnection is widely concerned for its close correlation with geomagnetic storms and substorms in the magnetosphere [1–4], and flares and coronal mass ejections (CMEs) in the solar atmosphere [5–7].

Because the plasmas in space are mostly collisionless, previous analytical calculations and simulations [8–11] have been mostly focused on collisionless magnetic reconnection in which they suggested that the Hall effect is the key to understanding fast magnetic reconnection in most plasma

environments. Experiments [12–14] and satellite observations [15, 16] also verify the existence of the Hall effect in fast reconnection. The classic magnetohydrodynamics (MHD) description of magnetic reconnection fails to predict the fast reconnection rate since the Hall physics must be included. Hence the Hall term is imperative to decouple the ion and electron dynamics. The ions and electrons break the frozen-in condition at different scales, forming the multiscale structure of the diffusion region. The onset of fast reconnection has been a long-standing complicated problem in the theory of magnetic reconnection [11, 17, 18]. Previous studies suggest that the triggering process involves the physics of kinetic Alfvén waves [19], whistler waves [20], and nonlinear multi-wave coupling [21]. It is helpful to explore the details of Hall physics to gain a deeper understanding and potentially solve this puzzle. It was found that the Hall effect accelerates the tearing instability and facilitates the onset of fast reconnection [22]. Fast magnetic reconnection is firstly triggered on an electron

* Authors to whom any correspondence should be addressed.

scale [23], where the frozen-in condition is broken by the electron dynamics. Then the Hall effect bridges the physical process from the ion scale to the electron scale. In general, the final reconnection process involves ion dynamics on a global scale [11]. In the inflow region, the bipolar Hall electric field accelerates the ions merging into the reconnection site, thinning the reconnection layer to the scale of the ion diffusion length [24, 25]. When the accelerated electrons jet outward at the exhaust region [26], an out-of-plane quadrupole structure of the magnetic field, namely the Hall magnetic field, is formed [27]. Therefore, the quadrupole Hall magnetic field and the bipolar Hall electric field are characteristic signatures of the Hall effect in fast reconnection.

Nevertheless, when shifting our focus from the interplanetary plasmas to more various plasma environments, the role of the collision effect can be intriguing, for instance, in the lower solar atmosphere such as the photosphere and the chromosphere where neutral particles begin to take effect [28], and in the Martian magnetotail where dynamics of the heavy ions can affect the reconnection process effectively [29]. Moreover, magnetic reconnection in laboratory plasmas (e.g. tokamaks [30–32], reversed field pinch [14], spheromaks [33, 34], laser-plasma interaction [35], and dedicated reconnection facilities [12, 36–38]) is featured with various configurations and more adjustable parameter range from collisionless (Hall) to collisional (Sweet–Parker) regimes [39]. Experiments on the magnetic reconnection experiment (MRX) device [13, 40] have reported that the quadrupole Hall magnetic field decreases as the collisionality strengthens, but the underlying physics of why the Hall magnetic field is weakened by collision remains ambiguous. Former researchers imply the collisional-to-collisionless transition can be seen as a phase transition [39, 41, 42]. Daughton *et al* [43, 44] have investigated the process of the transition from the Sweet–Parker regime to the kinetic regime by kinetic simulations. The emergence of plasmoids and current sheet thinning to the ion scale is observed, while the Hall magnetic field and the Hall electric field are not described in the process. Now comes the question of how Hall magnetic reconnection will evolve when introducing collision effects. Stronger collision effects can result in larger classical resistivity, providing for the conditions of Sweet–Parker reconnection (i.e. resistive reconnection). Contrarily, weaker collisionality may result in a more Hall-like regime (i.e. kinetic regime). The key question is on what condition the Hall effects dominate and on what condition the collision effects take advantage. Understanding how collisions affect those Hall fields can provide a more lucid perspective of the Hall effects during magnetic reconnection.

The Hall magnetic field and the Hall electric field are known as the characteristic indicators of Hall effects. Our research aims to evaluate those Hall fields as indicators and attempts to find how and why the indicators change in the transition from one regime to the other.

To investigate the questions above, we conduct a series of particle-in-cell (PIC) simulations from collisionless to collisional. We focus on the reconnection that spontaneously arises from a Harris current sheet. Only the collision parameter (Lundquist number) is varied for all cases, while other

parameters remain the same. The detailed simulation setup is described in section 2. By examining the fields related to Hall effects over time, we present the time evolution of the quadrupole Hall magnetic field and the Hall electric field. Through comparison cases with different collisionality, influences of collisions on the Hall effects are also illustrated. Those results are shown in section 3. Finally, discussion and conclusions are given in section 4.

2. Simulation setup

We perform the 2.5D kinetic simulations using the EPOCH PIC code [45] which involves a Monte–Carlo module to calculate the Coulomb collisions. The electromagnetic field is updated by solving the Maxwell’s equations. The electron and ion motions are advanced in the electromagnetic field by solving their motion equations. Our simulations are conducted in a x – z plane, where the calculation box is $L_x \times L_z$ with $L_x = 100d_i$ and $L_z = 100d_i$. $d_i \equiv c/\omega_{pi}$ denotes the ion inertia length and $\omega_{pi} \equiv \sqrt{n_0 e^2 / \epsilon_0 m_i}$ is the ion plasma frequency. The x -boundaries are periodic and the z -boundaries are perfect electric conductor. The grid spacing is $\Delta x = \Delta z = 0.0625d_i$. The time step is $\Delta t = 0.0024\Omega_i^{-1}$, where $\Omega_i \equiv eB_0/m_i$ is the ion gyrofrequency. The mass ratio is $m_i/m_e = 40$. The speed of light is taken as $c = 9.04v_A$, where $v_A \equiv B_0/\sqrt{\mu_0 n_0 m_i}$ is the Alfvén velocity.

The initial condition is the Harris current sheet equilibrium without perturbations. The magnetic field is set to be $\mathbf{B} = B_0 \tanh(z/\delta) \mathbf{e}_x$ with no guide field. B_0 denotes the asymptotic magnetic field and δ is the half-width of the initial current sheet. We take $\delta = 0.5d_i$ for all cases in our simulations. The initial plasma density is $n = n_0 \text{sech}^2(z/\delta) + n_b$ for both electrons and ions, where n_0 is the initial plasma density at the center of the Harris current sheet. A uniform background density of $n_b = 0.3n_0$ is applied. The ion temperature is the same as the electron temperature at initialization.

The simulation setups above are applied for all cases. The only variable is the collision parameter, i.e. the Lundquist number $S \equiv \mu_0 v_A L / \eta$, where L is the characteristic length of reconnection; here we take $L = 100d_i$

$$\eta \equiv \frac{Ze^2 \sqrt{m_e} \ln \Lambda}{32 \epsilon_0^2 \sqrt{2\pi} T_e^{3/2}} \quad (1)$$

is the Spitzer resistivity calculated using the initial temperature at the center of the current sheet. Based on the Coulomb collision theory, the relationship between the Lundquist number and the corresponding mean free path can also be calculated

$$S = \frac{2}{\sqrt{3}} \sqrt{\frac{m_i}{m_e}} \sqrt{\frac{T_i}{T_e}} \frac{L}{\rho_i} \frac{\lambda_{\text{mfp}}}{d_i}. \quad (2)$$

The collision parameters for all cases are listed in table 1. The simulation data based on the setup above are openly available [46].

In the EPOCH PIC code, the collision is realized using a scattering algorithm based on the model presented by

Table 1. Collision parameters of calculation cases. The Lundquist numbers shown in the table are set in the middle of the current sheet during initialization. $\delta/\lambda_{\text{mfip}}$ is the ratio of the initial current sheet width ($\delta = 0.5d_i$ for all cases) and the mean free path of the particles (λ_{mfip}).

Case	Lundquist number	$\delta/\lambda_{\text{mfip}}$
A	∞	0
B	10^5	0.0073
C	5×10^4	0.0146
D	2×10^4	0.0365
E	8455	0.0864
F	3000	0.2434
G	1200	0.6086
H	625	1.1685
I	300	2.4343
J	150	4.8686

Nanbu and Yonemura [47] and Pérez *et al* [48]. For a specific Lundquist number, the corresponding central temperature and density of the current sheet can be calculated through equation (1), which are given as the initial condition in the code.

3. Results

3.1. Time evolution of Hall fields

We performed several PIC simulations with different Lundquist numbers varying from $S = 150$ to $S = \infty$, viz. collisionless, listed in table 1. Detailed simulation setups are in the Methods section. All cases except case J present signs of Hall magnetic reconnection, i.e. the quadrupolar magnetic field pattern near the X-line, a maximum reconnection rate at the scale of 0.1, and significant outflows that approach or exceed the Alfvén velocity. None of those are found in case J through the calculation time (approximately $500 \Omega_i^{-1}$). The reconnection rate of case J maintains the scale of 10^{-3} .

Firstly, we focus on the Hall reconnection process. Here we take case C as a typical example (shown in figure 1). Field components related to the Hall effect at several moments during Hall reconnection are plotted in figures 1(b)–(d). On the one hand, the quadrupolar Hall magnetic field B_y (figure 1(b1)) begins to form and rises with the outflowing current J_x (figure 1(d1)) after fast reconnection is triggered. Later the quadrupolar pattern is enhanced and reaches a maximum at $\Omega_i t = 75.8$ (figure 1(b3)) with the current density in the x -direction growing to the acme at the same time (figure 1(d3)). Then it expands to the pile-up region and the density becomes weaker (figures 1(b4) and (d4)). On the other hand, the z -component of the electric field, namely the Hall electric field, exists earlier than the onset of fast reconnection and maintains the bipolar pattern during the reconnection process (figures 1(c1)–(c4)).

To quantify the Hall effect in magnetic reconnection, we calculated three characteristic quantities closely related to the Hall effect, i.e. the Hall magnetic field B_{Hall} , the peak of the outflowing current $J_{x,\text{max}}$, and the Hall electric field E_{Hall} ,

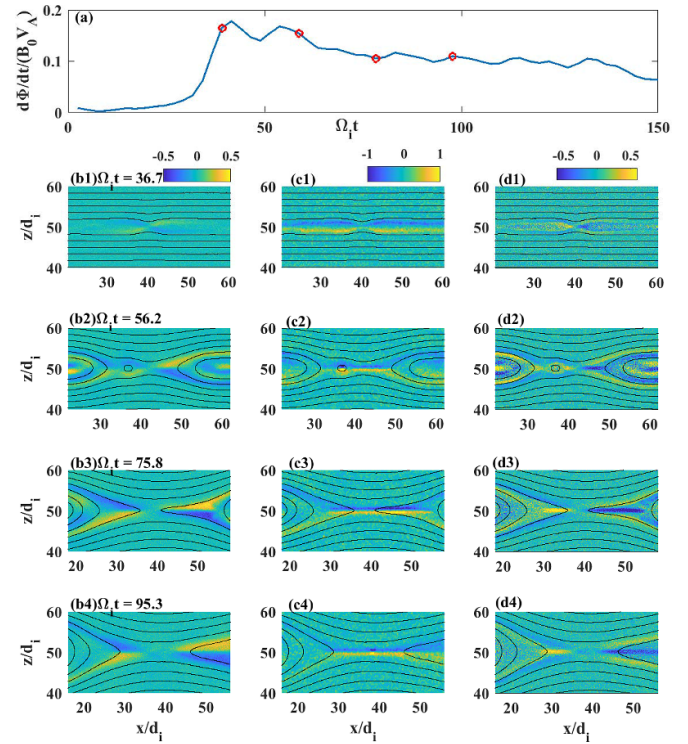


Figure 1. Field components related to Hall effects at different moments in case C. (a) Time evolution of reconnection rate. (b1)–(b4) the y -component of the magnetic field B_y , (c1)–(c4) the z -component of the electric field E_z , and (d1)–(d4) the x -component of the current J_x at different moments are shown. The black solid lines denote the magnetic field. The corresponding moments are plotted as red dots in (a).

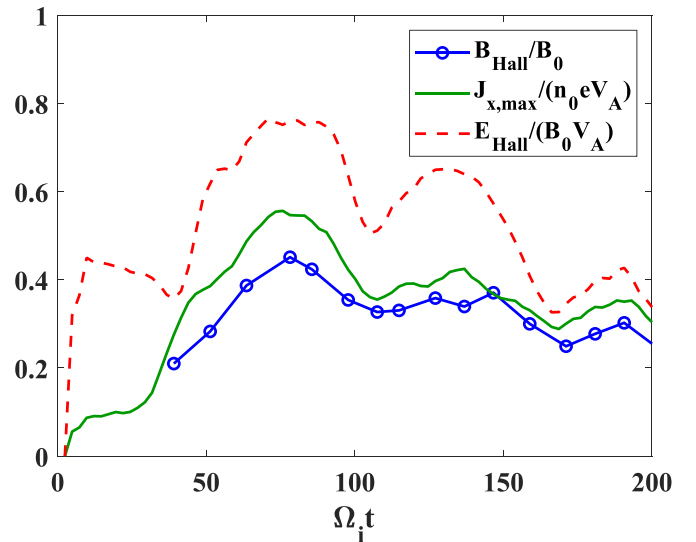


Figure 2. Time evolution of the Hall magnetic field amplitude (blue line with circles), the maximum outflowing current (green solid line), and the Hall electric field (red dashed line).

shown in figure 2. Those quantities are all smoothed and averaged over $1 \Omega_i^{-1}$ to reduce the noise. The decoupling of ion and electron motions forms the in-plane current, generating the out-of-plane Hall magnetic field. Thus, we take the

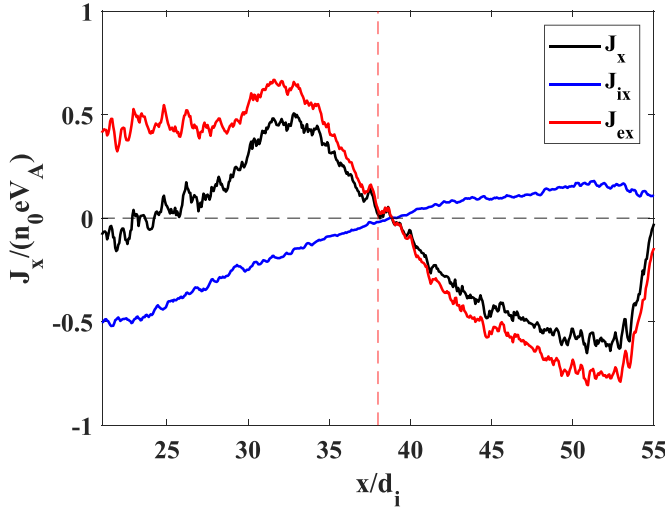


Figure 3. The outflowing current components near the X-line of case C at $\Omega_i t = 75.8$. The red dashed line represents the position of the X-line. The total electric current density (black), the ion current density (blue), and the electron current density (red) are plotted along the $z = 0$ line. Those current densities are averaged in the $z = \pm 0.5d_i$ range to reduce the noise.

maximum amplitude of the quadrupolar magnetic field B_y as the Hall magnetic field in our simulations, which is only calculated since $\Omega_i t = 39$, when the quadrupole pattern is obviously formed. In the ion diffusion region, the Hall term $(\mathbf{J} \times \mathbf{B})/ne$ in the generalized Ohm's law, mainly composed of the $J_y B_x/ne$ component at the vicinity of the X-line, is far greater than the convection term and other non-frozen-in terms. In addition, it has been shown that the E_z component is predominantly electrostatic [49], which results from charge separation. Consequently, the maximum absolute value of E_z around the X-line along the z -direction can be taken as the Hall electric field.

The Hall magnetic field evolves with the outflow current J_x synchronously, while the trend of the Hall electric field is inconsistent with the outflow before $\Omega_i t = 39$ (see the red dashed line in figure 2), which is already formed before the onset of the fast reconnection. The outflow near the X-line (within $8d_i$) is mainly attributed to the electron current J_{ex} (the red solid line in figure 3). The relationship between the magnetic field and the current density can be described by equation (3)

$$\nabla \times \mathbf{B} = \mu_0 \mathbf{J}. \quad (3)$$

The displacement current term is neglected in the steady-state approximation. In our specific x - z plane, equation (3) is reduced to

$$\frac{\partial B_y}{\partial z} \approx \frac{B_{\text{Hall}}}{\delta_{\text{Hall}}} = \mu_0 J_x. \quad (4)$$

The δ_{Hall} denotes the characteristic width of the quadrupole pattern, which can be approximated as the width of the current sheet. B_{Hall} is roughly proportional to the current J_x formed in the exhaust region of reconnection; this tendency is certified in

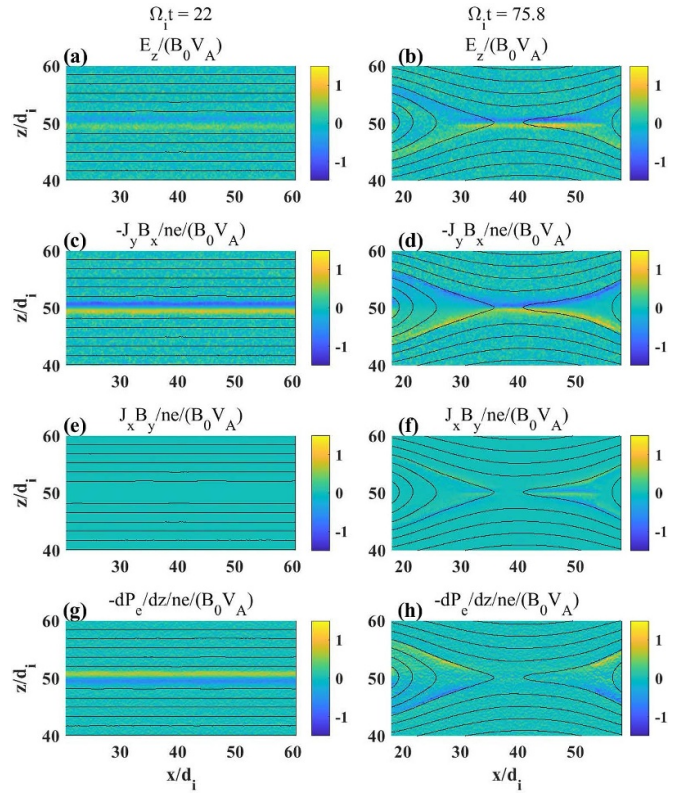


Figure 4. The contour of the normalized z -components in the general Ohm's law (equation (5)) for case C at two different times. The panels in the first column are snapshots of field components at $\Omega_i t = 22$, before the onset of fast reconnection. The second column is at $\Omega_i t = 75.8$, when Hall reconnection is well-developed. (a and b) z -component of the electric field E_z (i.e. the Hall electric field) and two components in the Hall term (c and d) $-J_y B_x / (ne)$ and (e and f) $J_x B_y / (ne)$. (g and h) The z -component of the electron pressure gradient term $-(\nabla P_e)_z / ne$. The black solid lines denote the magnetic field lines.

figure 2. When J_x peaks, B_{Hall} reaches the maximum as well, proving that the Hall magnetic field is an explicit sign of Hall reconnection.

Unlike the Hall magnetic field, the Hall electric field E_z emerges at the pre-reconnection stage (before $\Omega_i t = 39$). Here we try to figure out the evolution of the Hall electric field through decomposing the general Ohm's law in the z -direction

$$E_z + (\mathbf{V} \times \mathbf{B})_z = \frac{1}{ne} (-J_y B_x + J_x B_y) - \frac{1}{ne} \frac{dP_e}{dz}. \quad (5)$$

We decompose the Hall term in the general Ohm's law into two terms. The first term $-J_y B_x / ne$ is naturally formed by the initial Harris current sheet configuration. The second term $J_x B_y / ne$ is composed of outflow current and the Hall magnetic field. We focus on the ion diffusion region, where the Hall effects dominate. The $\mathbf{V} \times \mathbf{B}$ term is small in this region. The electron inertial term and the off-diagonal components of the electron pressure tensor are also omitted because they are only dominant in the electron diffusion region. The remaining components of case C are plotted in figure 4 before ($\Omega_i t = 22.0$, the first column in figure 4) and after ($\Omega_i t = 75.8$, the second column in figure 4) the onset of fast reconnection.

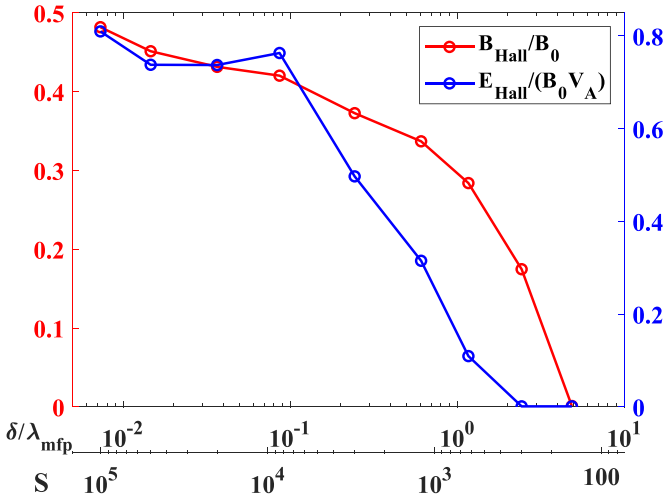


Figure 5. The maximum Hall magnetic field (blue) and the Hall electric field (red) versus the collision parameters (i.e. the ratio of the initial current sheet half-width δ to the mean free path λ_{mfp} and the Lundquist number S). The x -axis employs the logarithmic coordinates; thus, case A is not shown in the figure for $\delta/\lambda_{\text{mfp}} = 0$ and $S = \infty$.

Before the onset, the bipolar electric field structure is formed (figure 4(a)). The Hall component $-J_y B_x/ne$ (figure 4(c)) and the electron pressure gradient term (figure 4(g)) present the adverse bipolar pattern, yet the Hall term is apparently larger, meaning the central thermal pressure cannot contend against the upstream magnetic pressure, allowing the electric field to drive the ions along with the magnetic flux into the reconnection site. After fast reconnection is triggered, the bipolar electric field grows more intense and expands to the separatrices (figure 4(b)). Still, the dominant part is the component of $-J_y B_x/ne$ (figure 4(d)). The $J_x B_y/ne$ term exists close to the neutral line at the exhaust region (figure 4(f)), corresponding to the coefficient of the Hall magnetic field and the outflowing current. The electron pressure gradient formerly at the reconnection site shifts to four arms of the separatrices, which can no longer hinder the inflow of the magnetic flux.

3.2. Effects of collision on Hall fields

The features of Hall fields described above for case C also hold for other cases (except the collisional reconnection in case J), the same means can be applied to evaluate the Hall fields for other cases. Once we find out the maximum Hall magnetic field and the Hall electric field during reconnection, we can compare the maximum B_{Hall} and E_{Hall} for all cases with varying collisionality, shown in figure 5. The Coulomb collision can be represented by either the mean free path or the Lundquist number, both labeled at the x -axis. The maximum Hall B field descends as the collisionality becomes stronger (shorter mean free path and smaller Lundquist number S). This tendency is consistent with the experimental results [13].

For detailed comparison, the maximum Hall magnetic field patterns for cases C, H, I, and J are plotted in figure 6. When the collisionality becomes stronger, the Hall magnetic field

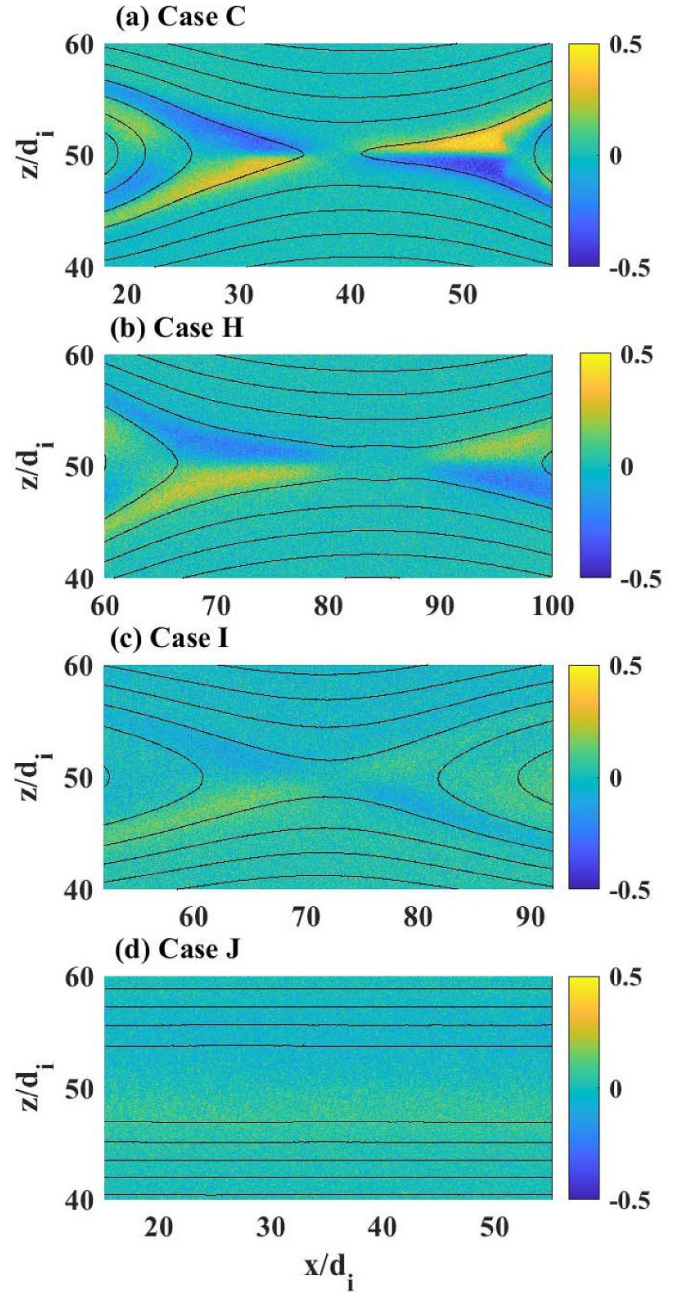


Figure 6. The B_y component of the magnetic field of cases C, H, I, and J. The contours of cases C, H, and I are plotted at the time when B_y peaks. A typical time ($\Omega_i t = 73$) is chosen for case J as it remains a quasi-steady-state over the simulation process. The black solid lines denote the magnetic field lines.

structure is weaker but maintains an identifiable quadrupolar structure until fast reconnection is not triggered in case J. The impairing Hall magnetic field implies that collision can reduce the electron outflow.

We notice that the Hall electric field diminishes earlier than the Hall magnetic field (cases F–J) when $S < 10^4$ (see figure 5). To quantify the reduction of the electric field, we plot the z -components (the inflow direction) of terms in the generalized Ohm's law in figure 7 (also for cases C, H, I, and J). For the typical Hall reconnection (case C), the E_z component

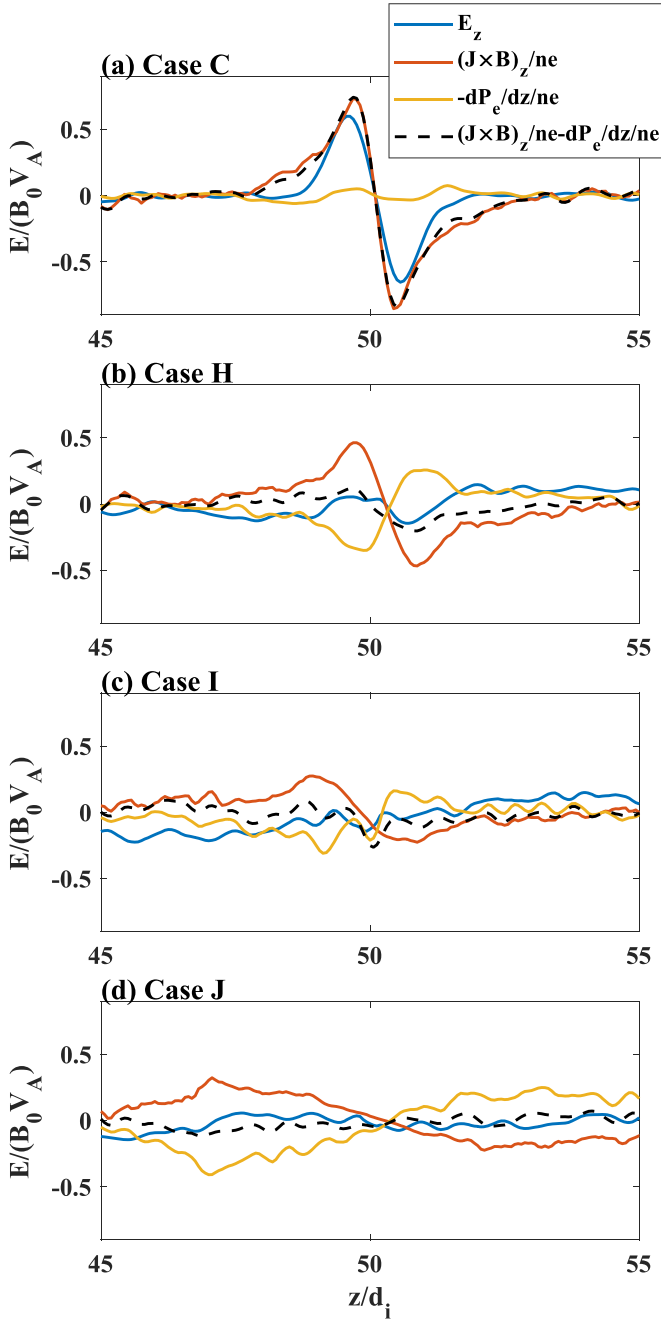


Figure 7. Z-components of terms in the generalized Ohm's law at the X-line in the inflow region of cases C, H, I, and J. The components are averaged over $\pm 0.5d_i$ in the x -direction. (Blue) The electric field component E_z , (red) the Hall term, (orange) the electron pressure gradient term, (black dashed) the sum of the Hall term and the electron pressure gradient term. Those terms of cases C, H, and I are plotted at the time when B_y peaks. A typical time ($\Omega_i t = 73$) is chosen for case J as it remains a quasi-steady-state over the simulation process.

is dominated by the Hall term $\mathbf{J} \times \mathbf{B}/ne$. As the collisionality grows stronger, the Hall term decreases because the decoupling between the ions and electrons becomes weak. Further, the electron pressure rises slightly due to the heating effect

by collision. For cases I and J (figures 7(c) and (d)), the Hall term (corresponding to the Lorentz force) is almost balanced by the electron pressure gradient term, causing the reduction and even disappearance of the Hall electric field. It is also noticed that the peaks of the Hall term and the electron pressure term expand to a wider range in case J (figure 7(d)). This is also evidence of the expansion of the current sheet width due to collision, i.e. the weak Lorentz force fails to drive the plasma flux and the magnetic field lines into the reconnection region.

4. Conclusions and discussion

In conclusion, the quadrupolar Hall magnetic field is approximately proportional to the outflow electron current density in the exhaust region, which well reflects the Hall physics in reconnection. On the other hand, the Hall electric field is related to the non-equilibrium of the pressure gradient force and the Lorentz force in the inflow direction even before the onset of fast reconnection. As the collisionality becomes stronger, the mean free path reduces to the scale of sub-ion inertial length, depressing the charge separation, thus the Lorentz force (Hall term) descends; together with the heating effect by collision, the thermal pressure increases, corresponding to the decline of the Hall electric field. Besides, the collision effect can reduce the electron outflow current density, impairing the quadrupole Hall magnetic field. We noticed that the electric field diminishes more easily than the quadrupolar Hall magnetic field when the collisionality grows stronger.

The quadrupolar magnetic field structure certifies the existence of the Hall effect. While the bipolar electric field pattern can be harder to assess especially when the collisionality becomes stronger. The discrepancy between the electric field and the magnetic field may arise from their generation mechanism. The Hall electric field requires charge separation in space. The ion–electron collision brings the momentum and energy exchange between two types of particles, and mixes up ions and electrons at the scale of the mean free path. When the mean free path reduces below the ion inertial scale (cases G, H, and I in table 1), ions cannot complete a gyromotion or meandering path around the neutral line in a mean collision interval. At this scale, the ions become partially unmagnetized due to collision, so that they will diffuse to counteract charge separation. The diffusion time scale ($\sim \delta/v_{thi}$) is approximately the same order as the ion cyclotron period. On the other hand, at the exhaust region, electrons can still be accelerated and jet outward at the order of the electron Alfvén speed V_{Ae} . Even though the unmagnetized ions attempt to follow the electron jets, they cannot be accelerated to V_{Ae} by electron–ion collision. Therefore, the Hall current and Hall magnetic field can still be generated without charge separation in space, they only require the decoupling of the electron flux and ion flux in the phase space at the exhaust region, which makes the Hall magnetic field structure easier to hold. Only when the mean

free path falls below the electron inertial length the diffusion is strong enough to break the electron frozen-in condition and totally erase the decoupling between electron and ion motion (see case J).

We applied a reduced mass ratio of $m_i/m_e = 40$ in our research. For the physical mass ratio, the gap between the ion inertial length and the electron inertial length becomes wider, resulting in a wider parameter space of the intermediate regime between the Hall regime and the collisional regime. This makes the regime easier to observe in experiments. The temperature ratio between ions and electrons can also alter this intermediate regime as the collision parameters are determined by the temperature. In this work, we set the initial ratio $T_i/T_e = 1$ for simplicity, so that the ion mean-free-path and the electron mean-free-path are identical. Altering the temperature ratio can be complicated, which will be discussed in future work.

Our simulation results can be mapped into the single X-line collisionless to collisional phase in Ji and Daughton's phase diagram [39], though the intermediate regime is not shown in the diagram. The effective plasma size in our simulations is fixed as $L/d_i = 100$, which is too short to generate plasmoids. Hence, the multiple X-line phase (or the plasmoid phase) in Daughton's simulation [50] is not discovered in our results. Occasional temporary secondary magnetic islands can be noticed near the X-line (e.g. figures 1(e)–(g) and (n)–(p)), which may enhance or impair the local Hall fields but its impact on the reconnection process can be negligible due to its randomness and short lifespan.

Our results certify that the quadrupolar Hall magnetic field can be a significant feature in identifying Hall reconnection, which can facilitate the experiments to evaluate whether Hall physics occurs. Those findings can help us further understand the effects of collision on the reconnection rate and energy conversion process.

Data availability statement

The data that support the findings of this study are openly available at the following URL/DOI: <https://doi.org/10.57760/sciencedb.13595>.

Acknowledgments

This work was supported by National Key Research and Development Program of China (No. 2022YFA1604600), the NSFC Grants 42174181 and 42274196, and the Strategic Priority Research Program of Chinese Academy of Sciences, Grant No. XDB 41000000. This work utilized the EPOCH PIC code, which was in part funded by the UK EPSRC Grants EP/G054950/1, EP/G056803/1, EP/G055165/1 and EP/M022463/1. Computer resources were provided by the Hefei Advanced Computing Center of China. Grateful acknowledgment is made to the data resources from 'National Space Science Data Center, National Science & Technology Infrastructure of China. (www.nssdc.ac.cn)'.

ORCID iDs

Yukang Shu  <https://orcid.org/0000-0003-0691-1596>

Kai Huang  <https://orcid.org/0000-0003-3630-309X>

References

- [1] Baker D N, Pulkkinen T I, Angelopoulos V, Baumjohann W and McPherron R L 1996 *J. Geophys. Res.* **101** 12975–3010
- [2] Angelopoulos V et al 2008 *Science* **321** 931–5
- [3] Kepko L, McPherron R L, Amm O, Apatenkov S, Baumjohann W, Birn J, Lester M, Nakamura R, Pulkkinen T I and Sergeev V 2015 *Space Sci. Rev.* **190** 1–46
- [4] Lu Q, Fu H, Wang R and Lu S 2022 *Chin. Phys. B* **31** 089401
- [5] Lin J and Forbes T G 2000 *J. Geophys. Res.* **105** 2375–92
- [6] Bárta M, Büchner J, Karlický M and Kotrč P 2011 *Astrophys. J.* **730** 47
- [7] Takasao S, Asai A, Isobe H and Shibata K 2012 *Astrophys. J.* **745** L6
- [8] Terasawa T 1983 *Geophys. Res. Lett.* **10** 475–8
- [9] Drake J F and Burkhart G R 1992 *Geophys. Res. Lett.* **19** 1077–80
- [10] Mandt M E, Denton R E and Drake J F 1994 *Geophys. Res. Lett.* **21** 73–76
- [11] Birn J et al 2001 *J. Geophys. Res.* **106** 3715–9
- [12] Tharp T D, Yamada M, Ji H, Lawrence E, Dorfman S, Myers C E and Yoo J 2012 *Phys. Rev. Lett.* **109** 2–6
- [13] Ren Y, Yamada M, Gerhardt S, Ji H T, Kulsrud R and Kuritsyn A 2005 *Phys. Rev. Lett.* **95** 055003
- [14] Ding W X, Brower D L, Craig D, Deng B H, Fiksel G, Mirnov V, Prager S C, Sarff J S and Svidzinski V 2004 *Phys. Rev. Lett.* **93** 4–7
- [15] Øieroset M, Phan T D, Fujimoto M, Lin R P and Lepping R P 2001 *Nature* **412** 414–7
- [16] Wang R et al 2017 *Phys. Rev. Lett.* **118** 175101
- [17] Singh N 2012 *Phys. Rev. Lett.* **109** 145001
- [18] Cassak P A and Shay M A 2012 *Space Sci. Rev.* **172** 283–302
- [19] Dai L, Wang C, Zhang Y, Lavraud B, Burch J, Pollock C and Torbert R B 2017 *Geophys. Res. Lett.* **44** 634–40
- [20] Deng X H and Matsumoto H 2001 *Nature* **410** 557–60
- [21] Huang F and Feng X 2018 *Geophys. Res. Lett.* **45** 11572–80
- [22] Hosseinpour M, Bian N and Vekstein G 2009 *Phys. Plasmas* **16** 012104
- [23] Liu D, Lu S, Lu Q, Ding W and Wang S 2020 *Astrophys. J.* **890** L15
- [24] Uzdensky D A and Kulsrud R M 2006 *Phys. Plasmas* **13** 062305
- [25] Litvinenko Y E 2009 *Astrophys. J.* **694** 1464–70
- [26] Fu X R, Lu Q M and Wang S 2006 *Phys. Plasmas* **13** 1–7
- [27] Lu Q et al 2010 *J. Geophys. Res.* **115** A11208
- [28] Chae J and Litvinenko Y E 2021 *Res. Astron. Astrophys.* **21** 232
- [29] Wang L et al 2023 *Geophys. Res. Lett.* **50** e2023GL104996
- [30] Wesson J A 1990 *Nucl. Fusion* **30** 2545–9
- [31] Yamada M, Levinton F M, Pomphrey N, Budny R, Manickam J and Nagayama Y 1994 *Phys. Plasmas* **1** 3269–76
- [32] Nagayama Y, Yamada M, Park W, Fredrickson E D, Janos A C, McGuire K M and Taylor G 1996 *Phys. Plasmas* **3** 1647–55
- [33] Matthaeus W H, Cothran C D, Landreman M and Brown M R 2005 *Geophys. Res. Lett.* **32** L23104
- [34] Yamasaki K et al 2015 *Phys. Plasmas* **22** 101202

- [35] Dong Q L *et al* 2012 *Phys. Rev. Lett.* **108** 1–6
- [36] Yamada M and Ji H 2010 *Proc. Int. Astron. Union* **6** 10–17
- [37] Sang L, Lu Q, Xie J, Fan F, Zhang Q, Ding W, Zheng J and Sun X 2022 *Phys. Plasmas* **29** 102108
- [38] Fan F, Xie J, Zhang Q, Sang L and Ding W 2019 *Chin. Phys. Lett.* **36** 015201
- [39] Ji H and Daughton W 2011 *Phys. Plasmas* **18** 111207
- [40] Yamada M, Ren Y, Ji H, Breslau J, Gerhardt S, Kulsrud R and Kuritsyn A 2006 *Phys. Plasmas* **13** 052119
- [41] Jara-Almonte J and Ji H 2021 *Phys. Rev. Lett.* **127** 1–6
- [42] Daughton W and Roytershteyn V 2012 *Space Sci. Rev.* **172** 271–82
- [43] Daughton W, Roytershteyn V, Albright B J, Karimabadi H, Yin L and Bowers K J 2009 *Phys. Plasmas* **16** 072117
- [44] Daughton W *et al* 2011 *AIP Conf. Proc.* **1320** 144–59
- [45] Arber T D *et al* 2015 *Plasma Phys. Control Fusion* **57** 113001
- [46] Shu Y *et al* 2023 *National Space Science Data Center* (<https://doi.org/10.57760/sciencedb.13595>)
- [47] Nanbu K and Yonemura S 1998 *J. Comput. Phys.* **145** 639–54
- [48] Pérez F, Gremillet L, Decoster A and Drouin M 2012 *Phys. Plasmas* **19** 32509
- [49] Lu S *et al* 2021 *J. Geophys. Res.* **126** e2021JA029550
- [50] Daughton W, Roytershteyn V, Albright B J, Karimabadi H, Yin L and Bowers K J 2009 *Phys. Rev. Lett.* **103** 1–4